A multi-channel TMS system enabling accurate stimulus orientation control during concurrent ultra-high-field MRI for preclinical applications

Victor H. Souza[a,b§*], Heikki Sinisalo [a§], Juuso T. Korhonen[a], Jaakko Paasonen[c], Mikko Nyrhinen[a], Jaakko O. Nieminen[a], Maria Koponen[a], Mikko Kettunen[c], Olli Gröhn[c], Risto J. Ilmoniemi[a]

[a] Department of Neuroscience and Biomedical Engineering, Aalto University School of Science, Espoo, Finland.

[b] School of Physiotherapy, Federal University of Juiz de Fora, Juiz de Fora, MG, Brazil.

[c] A. I. Virtanen Institute for Molecular Sciences, University of Eastern Finland, Kuopio, Finland.

[§] Equal contribution

*Corresponding author:

Department of Neuroscience and Biomedical Engineering

Aalto University School of Science

P.O. Box 12200, FI-00076 AALTO, Finland

Keywords

Transcranial magnetic stimulation, Multi-coil TMS, Multi-locus TMS, Multi-channel TMS, Orientation sensitivity, Automated brain stimulation, TMS-fMRI, fMRI, Rat, Animal, Magnetic resonance imaging

Abstract

Background: Monitoring cortical responses to neuromodulation protocols on preclinical models can elucidate fundamental mechanisms of brain function. Concurrent brain stimulation and imaging is challenging, usually compromising spatiotemporal resolution, accuracy, and versatility.

Objective: We aimed to (1) develop and characterize a multi-channel transcranial magnetic stimulation (TMS) system with electronic control of neuromodulation parameters in a magnetic resonance imaging (MRI) environment, (2) characterize the interplay between the mTMS system and the MRI recordings, and (3) verify how different TMS pulse orientations evoke distinct muscle responses in an anesthetized rat.

Methods: The multi-channel TMS system was designed using materials and electromagnetic safety mechanisms for compatibility with a 9.4-T scanner for small-animal MRI. To deliver the stimulation, we created a 2-coil transducer enabling electronic control of the induced electric field orientation in the rat's brain. The MRI compatibility was verified with a radiofrequency transceiver coil measuring MRI signals and the presence of imaging artifacts due to the stimulation pulses. We also investigated the effect of the multi-channel TMS pulse orientation on the motor responses of an anesthetized rat.

Results: We showed that the stimulation pulses do not affect the anatomical imaging quality, and imaging signals are disrupted only if recorded before 10 ms after pulse delivery. Without physically rotating the coils, we demonstrated that the rat's motor responses considerably depended on the E-field orientation.

Conclusion: Our system enables electronically targeted brain stimulation and neuroimaging, opening a possibility for investigating fundamental mechanisms of network brain functions in healthy animals and preclinical models of neurological disorders.

Introduction

Brain processes and diseases engage multiple cortical and subcortical regions that interact in a timely and orchestrated manner, forming complex interconnected networks [1]. Instead of focusing on specific areas of the cortex, we need to understand brain function at the network level [2–5]. Brain networks are observed across species, which makes preclinical experiments relevant for investigating biomarkers and the effects of treatments in pharmacologically, surgically, and genetically induced disease models [6–10]. In this context, transcranial magnetic stimulation (TMS) offers a non-invasive way of evoking targeted brain activation, and in combination with functional neuroimaging, it presents a powerful tool for assessing cognition and behavior [3,11–16] and for optimizing therapeutic outcomes [17,18]. While TMS can modulate neuronal activity through processes like long-term potentiation and depression [8,19,20], neuroimaging methods, such as positron emission tomography (PET) [21–26], electroencephalography (EEG) [12,27–30], and functional magnetic resonance imaging (MRI) [14,16,31], provide spatial and temporal information on the underlying brain activity. EEG has high temporal resolution but offers limited spatial specificity, especially with rodents, and while PET provides higher spatial specificity than EEG, it requires the use of radioactive tracers, hindering large-population studies. In turn, modern ultra-high-field MRI scanners offer superior spatial resolution compared to PET and EEG, enabling non-invasive network-level investigations of healthy and diseased brains [5,13,14,32].

Combining TMS with MRI in a preclinical setting poses significant technical challenges [33,34]. For instance, the MRI bore's restricted space and the setup constraints, such as the TMS coil positioning apparatus [35], require the operator to frequently remove the subject from the scanner to adjust the stimulation parameters. Thus, designing protocols to engage the brain networks with subsequent pulses on different loci or orientations with millisecond-scale intervals is impossible with traditional instruments [36,37]. Moreover, the interaction between the high static magnetic field and stimulation current in the TMS coil windings leads to high mechanical stress, causing fractures to the coil structure (see Supplementary Video) and potentially exposing the subject to hazards [14,38]. The development of multi-locus TMS (mTMS) has enabled electronic control of the induced electric field orientation and location in the human brain with resolutions exceeding 1° and 1 mm, respectively [39–41]. This makes mTMS suitable for automated and highly accurate stimulus targeting inside the scanner bore. Recently, a functional MRI coil array has been developed for human mTMS–MRI applications [42]. However, existing mTMS–MRI instrumentation has not been designed with mechanical properties and dimensions applicable to preclinical ultra-high-field MRI settings.

Here we aimed to develop an MRI-compatible mTMS system tailored for preclinical research. Also, our goal was to develop a system that allows for real-time electronic control of the orientation and intensity of applied brain stimulation within the MRI scanner, seamlessly integrated with imaging sequences. This system would offer unique features and improvements over existing devices for humans [43,44], leading to significant breakthroughs in brain studies.

Material and Methods

mTMS power electronics and connectivity

This mTMS power electronics is a smaller, two-channel variant of our recently developed 6-channel mTMS system for human applications, described in our previous work [40]. We modified the human mTMS system design to comply with MRI safety and compatibility with minimal ferromagnetic parts from structural components to printed circuit boards (see the Supplementary Material for further details). Currently, the system consists of two independent channels (capable of controlling two coils), with support for adding a third channel. Each channel has an H-bridge module [45,46] (maximum voltage 1500 V), which drives a current pulse in a single coil in an mTMS transducer. To minimize the electrical interference during mTMS–MRI recordings, the charging of the high-voltage capacitors is interleaved with the MRI acquisitions through a triggering interface.

A notable change compared to our other mTMS devices is the split installation in the MRI setting (Fig. 1), with the power electronics and the control unit placed in different locations to maintain as noise-free an environment as possible. The power electronics cabinet was fixed to a corner inside the shielded room outside the 0.5 mT region, and the control unit was placed inside the operating room. The control unit communicates with the power electronics via fiberoptic links fed through a waveguide into the shielded room. The device cabinet was custom-made from aluminum profiles and panels, non-magnetic stainless-steel fasteners (A2 and A4 grades), and polyoxymethylene plastic mounting plates. The electronics were designed to default into a safe state during a sudden absence of power.

To enable fast prototyping of different transducer designs, we designed a connection box inside the MRI bore that allows a simple and safe connection of the coil cables to the cabinet with threaded copper rods and plastic plates for electrical insulation. The mTMS system supports the electronic recognition of transducers via microchips with unique identifiers and connections to digital temperature sensors that can be embedded into the transducer for temperature monitoring.

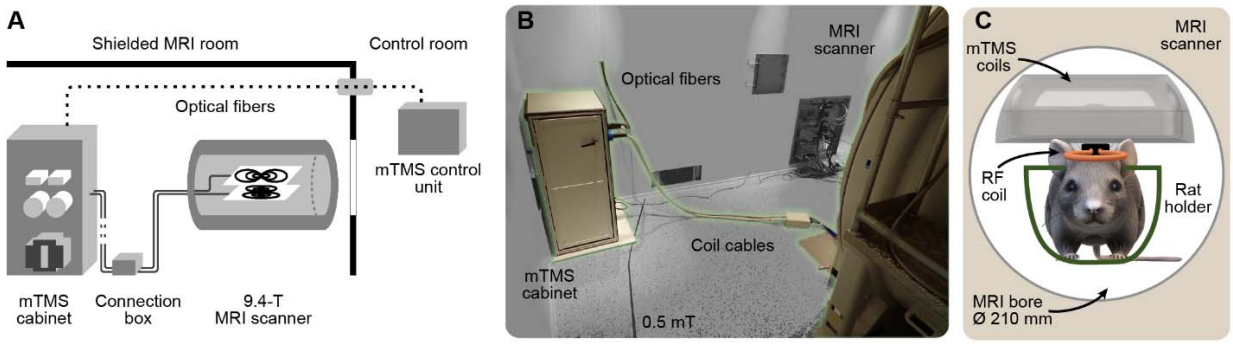

Fig. 1. The mTMS–MRI system. **(A)** Schematic of the mTMS system installation in the MRI shielded room. The optical fibers originating from the cabinet connect to the control unit inside the MRI control room. The mTMS transducer is placed in the MRI scanner bore and connects to the mTMS cabinet via two connection boxes, one of which is inside the MRI bore (not visible in the photo or the schematic). **(B)** Photo of the mTMS installation inside the MRI shielded room. **(C)** Illustration of the stimulation and recording coils inside the MRI bore with a 210-mm diameter. The radiofrequency (RF) coil is used for recording the MRI signals and is attached to the bottom of the case with the mTMS coils. A custom holder supports the animal and the coils (see Fig 3A).

mTMS transducer design, manufacturing, and calibration

For fast and accurate control of the induced peak E-field orientation in the rat's cortex, we designed and built a 2-coil transducer. The winding paths for the coils were generated with a

minimum-energy optimization method [46] with wire density constraints [47] implemented in MATLAB 2022a. First, we computed the induced E-field distribution for two coil orientations (0° and 90°) with a small commercial figure-of-eight coil model (MC-B35, MagVenture A/S, Denmark) on a triangular mesh (2568 vertices) located 15 mm away from a rat's spherical cortical surface (13.7-cm-radius sphere; 2562-vertex triangular mesh). For both orientations, we computed the corresponding minimum-energy surface current density in a rectangular plane section (19-cm long and 9.5-cm wide; 1953-vertex triangular mesh) that induces an E-field distribution with similar focality and intensity to the commercial coil model. We defined the dimensions of the rectangular plane section to fit inside a small gradient coil set (ø 11–12 cm) typically used in preclinical small-bore MRI systems. For the 0° and 90° coil orientations, we performed the optimization with the rectangular plane located at 15 and 20 mm from the cortical surface, respectively. Then, we decomposed the optimized surface current densities with singular value decomposition and discretized the coil winding paths from each surface current density in 14 isolines. This resulted in two orthogonal figure-of-eight coils (seven turns in each wing).

The 2-coil transducer is composed of two plates (bottom and top coils) and a case, all designed in SolidWorks 2018 (Dassault Systèmes SA, France). The bottom plate thickness is 7.0 mm (including a 2.0-mm-thick bottom), and the top plate is 10.0 mm thick (including a 5.0-mm-thick top). The bottom thickness corresponds to the material thickness below/above the wire grooves. The coil winding paths were machined in polycarbonate plates due to their excellent mechanical properties (75 MPa tensile strength and 2.4 GPa Young's modulus) necessary to withstand the high stress generated when applying TMS pulses with kiloampere-level currents inside an MRI bore with a 9.4-T static magnetic field. Each coil was wound with copper litz wire (1.7-mm diameter; 3-layer Mylar coating; Rudolf Pack GmbH & Co. KG, Germany) in the grooves of the

coil former (Fig. 2A) and crimped to the connection box placed inside the scanner's bore. The transducer plates were potted with a 2-component silicone-based elastomer (SYLGARD® 184, Dow Inc., USA) so that the 5-mm-thick top of the top former serves as a cover. The coil assembly is housed inside a custom case machined from polycarbonate with a 1-mm air gap to the bottom surface to reduce the mechanical coupling and a 1-mm-thick bottom for additional safety. See the Supplementary Material for further details.

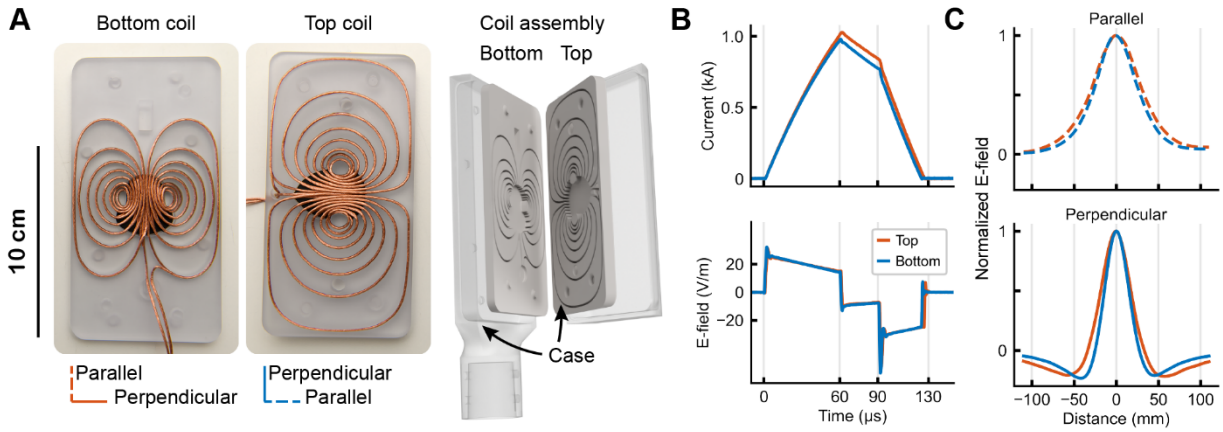

Fig. 2. The mTMS transducer, measured current waveforms and E-fields profiles. (**A**) The two figure-of-eight coils wound with litz wire in polycarbonate formers and a 3D model of the transducer assembly with the protective case. (**B**) Trapezoidal monophasic current (upper panel) pulse and its induced E-field waveform (lower panel) for the bottom and top coils inducing an E-field on a 70-mm radius spherical head model. (**C**) E-field profiles as indicated in (**A**) and measured with the TMS characterizer as in (**B**). These profiles are used to estimate the induced E-field focality in the direction parallel and perpendicular to the peak E-field.

After assembling the 2-coil transducer, we calibrated the electronic control of the induced E-field orientation. Using a TMS characterizer [48], we measured the E-field distributions at 1000 points over a spherical human cortex model with a 70-mm radius. The center of the transducer case

bottom was 85 mm from the center of the spherical head model. We computed the E-field intensity as its average norm on a trapezoidal monophasic current waveform's rising phase (60-µs long). For both coils, the monophasic pulse had phases lasting 60 (rise) and 30 µs (hold) and a falling phase of 32.5 and 35.2 µs for the bottom and top coils, respectively (Fig. 2B). The focality was computed as the full width at ~71% ($1/\sqrt{2}$) from the maximum of the perpendicular and parallel E-field profiles [48] (Fig. 2C).

We performed finite element simulations to assess the coil formers' stress distribution and mechanical durability. Simulations were done in COMSOL Multiphysics® 6.0 (COMSOL AB, Sweden) using a physically accurate 3D model of the transducer copper wiring and polycarbonate plates. The coil plates were placed inside a cylindrical air domain with a uniform magnetic field of 9.4 T representing the MRI bore. We fixed the plates in space by applying a spring boundary condition to one of their ends with a spring constant per unit volume of 1 N/m^3. The pure copper and polycarbonate material properties were obtained from the COMSOL material library and the Granta EduPack 2022 R1 database (ANSYS, Inc., USA), respectively.

mTMS–MRI characterization

To ensure the compatibility of the mTMS device and the MRI sequences, we characterized the effect of the mTMS transducer on the resonance frequency of a radiofrequency (RF) coil. MRI measurements were done with a 9.4-T magnet (bore diameter 31 cm) interfaced with a DirectDRIVE console (Agilent Technologies, Inc., USA) and with a 21-cm-inner-diameter gradient coil set.

In the first experiment, we applied a stimulation pulse and then acquired the free induction decay (FID) signal from a rat brain phantom after a single hard RF pulse. The RF excitation pulse was

given with a flip angle of 2° and a variable delay of 0–10 ms after the mTMS pulse (0.5 ms steps, 21 acquisitions with 2.5 s intervals) with a repetition time of 2500 ms. Slice selection was not used. For each mTMS–RF pulse delay, we tested eight stimulus orientations (−135°–180° in steps of 45°) with five intensities (0, 5, 8, 17, and 25% of maximum stimulator output). The RF pulse was delivered and recorded with a custom-made 400-MHz single-loop transceiver surface coil (Neos Biotec SL, Spain) consisting of a 22-mm inner diameter open loop connected to a separate tuning and matching box with a 6-cm-long coaxial cable (Fig. 3A). During manufacturing, the tuning and matching range of the RF coil was optimized while it was centered at the bottom of the mTMS transducer case. Additionally, we tested whether the powering of the mTMS system or connecting the mTMS transducer cables induced noise to the MRI's FID signal with 10 kHz and 208 kHz bandwidths without applying any mTMS pulses. Each set of FID measurements was repeated 10–20 times.

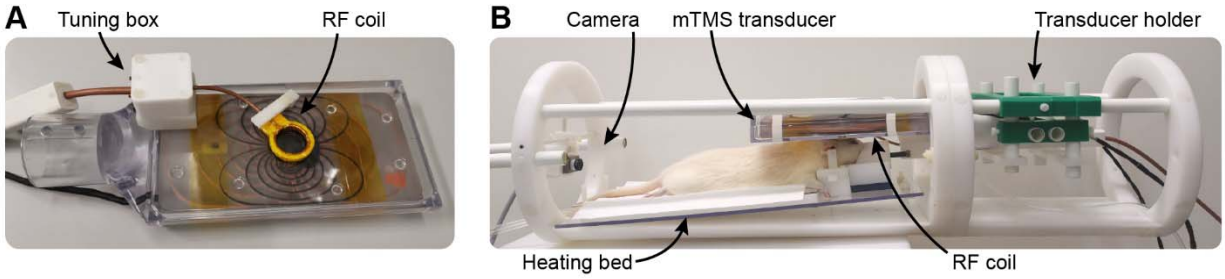

Fig. 3. Experimental setup for mTMS–MRI recordings. (**A**) Custom transceiver radiofrequency (RF) surface coil for recording the MRI signals attached to the center of the mTMS transducer case. (**B**) Custom holder used to for positioning the mTMS transducer and the MRI RF coil over the rat's head inside the MRI bore. An MRI-compatible camera was used to monitor the rat and set up during the whole session.

To study whether the mTMS setup induces any observable image distortion or signal during MRI, we performed structural imaging with the mTMS transducer on top of an anesthetized rat in a custom-made holder (Fig. 3B). For that, MRI data were acquired with two pulse sequences: multi-slice gradient echo (repetition time: 18 ms, echo time: 3 ms, flip angle: 20°, field-of-view: 60 mm × 60 mm, matrix size: 128 × 128) and spin echo (repetition time: 2000 ms, echo time: 30 ms, flip angle: 90°, field-of-view: 50 mm × 50 mm, matrix size: 256 × 256).

mTMS pulse acoustic noise

We characterized the sound pressure levels (SPL) generated by the mTMS pulses inside and outside the MRI bore. We measured the SPL with the open end of a 6.5-m long non-elastic tube in five locations: 4 cm below the mTMS transducer center and at a 1-m distance (far field), both measurements with the transducer inside and outside the MRI. The fifth location was with the mTMS transducer inside the MRI bore and the tube's open end in the MRI operation room (see Fig. 6A). In each location, we tested eight different E-field orientations (−135°–180° in steps of 45°) and six stimulation intensities (13% and 20%–100% in steps of 20% of maximum stimulator output; MSO) outside and eight intensities (10%–80% in steps of 10% MSO) inside the MRI bore. For high intensities (> 40% MSO), we covered the open end of the tube with a foam earplug to prevent the SPL from saturating the audio interface input. To avoid potential damage to the mTMS transducer due to the high Lorentzian forces involved, we limited the maximum intensity inside the MRI bore to 80% MSO. We also measured the SPL inside the control room with the mTMS transducer inside the bore using a 20%-MSO stimulation intensity. With the same intensity (20% MSO), we measured the effect of sound-insulating polyurethane foam (HiLo-N40, t.akustik, Germany) inside the MRI scanner and with the measurement tube at a 4-cm distance from the mTMS transducer bottom. The foam covered the MRI bore walls to

dampen the sound wave reflections. See the Supplementary Material for additional considerations.

The acoustic measurements were performed with a high-performance microphone (MKE 2 P-C, Sennheiser electronic GmbH & Co. KG, Germany) firmly attached to the end of a non-elastic tube (Tress Nobel, 40 bar, length 6.46 m, diameter 6 mm; Tricoflex) and digitized with a high-quality audio interface (RME Babyface Pro, Audio AG, Germany) controlled with custom software written in MATLAB 2022a. To accurately represent the acoustic noise SPL and frequency spectrum, we calibrated our measurements setup to the frequency range of 20–20,000 Hz at the Aalto Acoustics Laboratory (Aalto University, Finland).

Animal experiments

All animal procedures were approved by the Animal Experiment Board in Finland and conducted following the European Commission Directive 2010/63/EU guidelines. Neurophysiological experiments were performed with one adult male Wistar rat (400–600 g, RccHan®: WIST; Envigo RMS BV, Netherlands). Before the experiment, the rat was anesthetized with isoflurane (5% for induction, 2% for maintenance; Attane Vet 1000 mg/g, Piramal Critical Care BV, The Netherlands) in 30/70 O2/N2 carrier gas. Subsequently, anesthesia was switched to urethane (1250–1500 mg/kg i.p.; Sigma-Aldrich, Corp., USA). Sufficient depth of anesthesia was periodically confirmed by pinching the hind paw to observe the loss of limb contraction reflex. The rat was placed on a warm water circulation pad (37 °C; Corio CD, Germany) to maintain a normal body temperature.

Electrophysiological recordings

The head of the rat was fixed to our custom-made holder with ear and bite bars. The mTMS experiment started 30 minutes after the initial isoflurane anesthesia induction. EMG was recorded with disposable monopolar needle electrodes (SDN electrodes, stainless steel, Inomed GmbH, Germany) inserted into the belly of the biceps brachii muscle in the depilated forelimbs' left and right paws [49,50], as shown in Fig. 7C. The muscle belly was determined by palpation of the extended forelimb. The references were placed between each paw's second and third digits, and the ground was inserted in the tail's base. EMG signals were digitized with a NeurOne Tesla (Bittium Biosignals Ltd., Finland) with a 10 kHz sampling frequency and 2.5 kHz low-pass filtering.

We measured the effect of mTMS stimulus orientation on the amplitude and latency of motor-evoked potentials (MEPs) in the anesthetized rat outside the MRI bore. We first mapped the scalp location showing the highest MEP amplitudes with the mTMS transducer center about 0.5 cm lateral to the bregma and with stimulation intensity set to 67% MSO. Stimulation intensity and transducer location were adjusted until we detected MEPs on the contralateral biceps brachii muscle with visible limb twitches. With the transducer location fixed on the hotspot, we searched for the resting motor threshold (RMT) as the minimum stimulation intensity evoking at least three out of six MEPs with amplitude over 10 µV. The interval between consecutive pulses was 4.0–5.0 s. Lastly, we applied five single pulses with 110% of the RMT in each of eight stimulus orientations (−135°–180° in steps of 45°) over the hotspot at the left and right brain hemispheres while recording electromyography (EMG) from ipsi- and contralateral biceps brachii muscles.

Data analysis

MRI data: For analyzing the possible effects of the charger and cable noise and the effect of mTMS pulses on FID signal at different delays, a Fourier transform was performed, and the area under the curve (AUC) was calculated from the obtained spectra. Structural images processed with the Aedes software (aedes.uef.fi).

Acoustic data: The SPLs were calculated without weighting, i.e., Z-weighting [51], and as the average of the maximum SPLs across three separate mTMS pulses. The frequency spectrum was measured with a time window spanning 3 ms before and 40 ms after the pulse. The window length was approximately the time for the sound waves to travel twice the length of the measurement tube. Data samples of equal length were selected to calculate the frequency responses of the background noise. The samples were cosine filtered using the Tukeywin function to reduce artifacts from cutting the signal. Then, the filtered signal was used to create the 1/3 octave spectra. Measurements with the earplug were left out from the 1/3 octave spectra because the earplug altered the frequency responses.

MEP data: The MEP data were pre-processed by removing the pulse artifact from the continuous EMG signal using the TMS–EEG Artefact Removal tool (Version 1.0; Mega Elektroniikka Oy, Finland). The exponential decay model coefficients were set to 0 and band-pass filtered (3rd-order Butterworth filter, 15 and 1000 Hz cut-off frequencies). The EMG signal was divided into epochs from 5 ms before to 20 ms after the TMS pulse. MEPs were visually inspected, and epochs showing large artifacts, visible heartbeats, or having MEPs with peak-to-peak amplitude smaller than 10 µV were discarded from further analysis. In total, 33 MEPs were discarded from 80 recorded. We extracted the peak-to-peak amplitude from the remaining MEPs and manually annotated the onset latency.

All data were processed and analyzed with custom MATLAB scripts.

Results

MRI-compatible mTMS system

The resulting E-field spatial distributions for different orientations: 0° (bottom coil), 45° (both coils), and 90° (top coil) are shown in Fig. 4A. The bottom and top coil focalities in the direction perpendicular to the peak E-field were 21.4 and 25.7 mm, respectively; in the parallel direction, they were 37.8 and 42.9 mm, respectively. The top coil (16.7 µH, 133.0 mΩ) required approximately 37% more voltage than the bottom coil (12.7 µH, 121.82 mΩ) to induce the same E-field measured with the TMS characterizer.

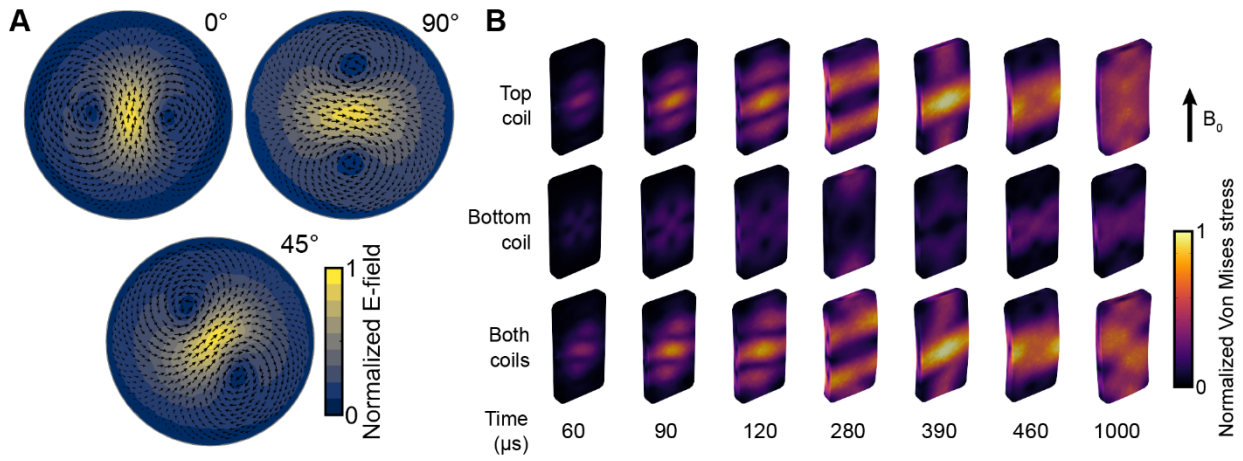

Fig. 4. The measured E-fields and simulated stress on the coil plates. (**A**) E-field spatial distribution measured with the TMS characterizer on a 70-mm radius spherical head model. The 0°, 90° and 45° correspond to the E-field orientation induced with the bottom coil, top coil, and both coils together, respectively. (**B**) Simulated stress distributions on the coil plates inside the MRI bore with a 9.4-T static magnetic field (B_0) when mTMS pulses were applied to each coil

separately (bottom and top) or to both coils simultaneously. The time is relative to the mTMS pulse onset as in the current waveform illustrated in Fig. 2B.

The stress was considerably higher for the top coil or with both coils fired together than for the bottom coil alone. The simulated peak stress values with a 100% MSO monophasic stimulation pulse (rise: 60 µs, hold: 30 µs, fall: 32.5 for the bottom and 35.2 µs for the top coil; see Fig. 2C) were 31.5 MPa, 70.9 MPa, and 71.4 MPa for the bottom coil, top coil, and both coils together, respectively. The change in stress distribution over time suggests that the coil plates vibrate, deform (Fig. 4B), and may eventually break. We took the results into account in the designs of the coil formers by increasing the thickness of the top plate compared to the bottom and by reinforcing the central region with a fluoroelastomer (black surface below the coil wires in Fig. 2A) to dampen the impact from the wires.

Interplay between mTMS and MRI

The close vicinity of the mTMS transducer shifted the RF coil's resonance frequency by 7 MHz, which was considered while optimizing the RF coil tuning and matching range. The mTMS system did not induce visually observable artifacts in the structural MRI. The mTMS transducer was not visible in the spin echo images, but it was faintly visible in the images obtained with the gradient echo sequence (Fig. 5A). The FID signal was distorted up to 3.0 and 6.0 ms after applying mTMS pulses with 8% and 25% MSO, respectively. The top coil alone (−90° orientation) caused the longest period of signal corruption in the FID power spectrum (up to 6.0 ms at 25% MSO pulse) while utilizing two coils simultaneously (e.g., a pulse in 45° orientation) caused the shortest period of signal corruption (up to 4.0 ms) (Fig. 5B–C). The presence of active but non-stimulating mTMS electronics affected the FID signal only minimally with 10 kHz (difference in AUC < 0.001 %) or 208 kHz (difference in AUC < 0.01 %) bandwidths.

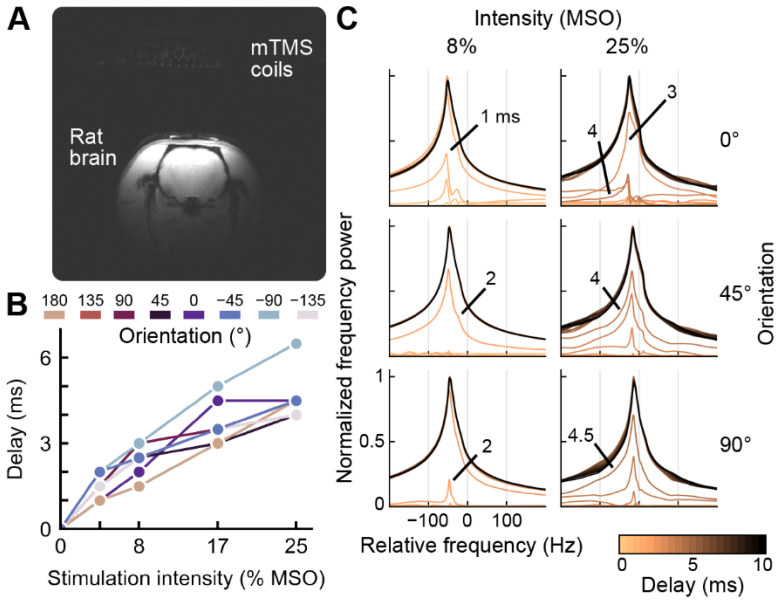

Fig. 5. Effect of mTMS pulse on the MRI signal. (**A**) Anatomical MRI taken with the mTMS transducer on top of the rat brain. The image brightness was slightly increased to make the mTMS coil windings visible. (**B**) Minimum delay between the mTMS pulse and the RF excitation pulse to obtain an artifact-free FID signal at different E-field orientations. Stronger intensities require longer delays which also depend on the induced E-field orientation. Stimulation intensities are measured as % of the maximum stimulator output (MSO). (**C**) MRI signal normalized power spectra recorded with multiple mTMS pulse intensities, orientations, and delays relative to the RF pulse. The black line represents the spectrum without an mTMS pulse. The numbers indicate the longest delay (in milliseconds) resulting in a corrupted power spectrum. At 0° orientation and with a stimulation intensity of 25 % MSO, the 4-ms delay showed a more corrupted spectrum than a 3-ms delay.

The peak SPL measured outside the MRI bore (without the B_0 field) was 142 dB(Z) at a 180° stimulus orientation and with 100% MSO stimulation intensity (Fig. 6B). Inside the bore, the highest peak SPL was 167 dB(Z), measured with a 0° pulse orientation (earplug as a dampener)

using 80% MSO stimulus intensity. The presence of the static magnetic field increased the SPLs by 44 dB(Z) on average, with stimulation intensities of 20% and 40% MSO (Fig. 6C). The effect of orientation across all stimulation intensities was 9 dB(Z) on average, 0° being the loudest and −90° the quietest (Fig. 6D). In the control room, SPLs were below 85 dB(Z), and it was not possible to distinguish them from the background noise with our measurement system. Thus, the noise is reduced by at least 60 dB from the scanner center to the control room. The sound-insulating foam lowered the peak SPL measured below the coil by an average of 4 dB(Z). At a 1-m distance, the peak SPLs inside and outside the bore were attenuated by 20 dB(Z) and 23 dB(Z) on average, respectively.

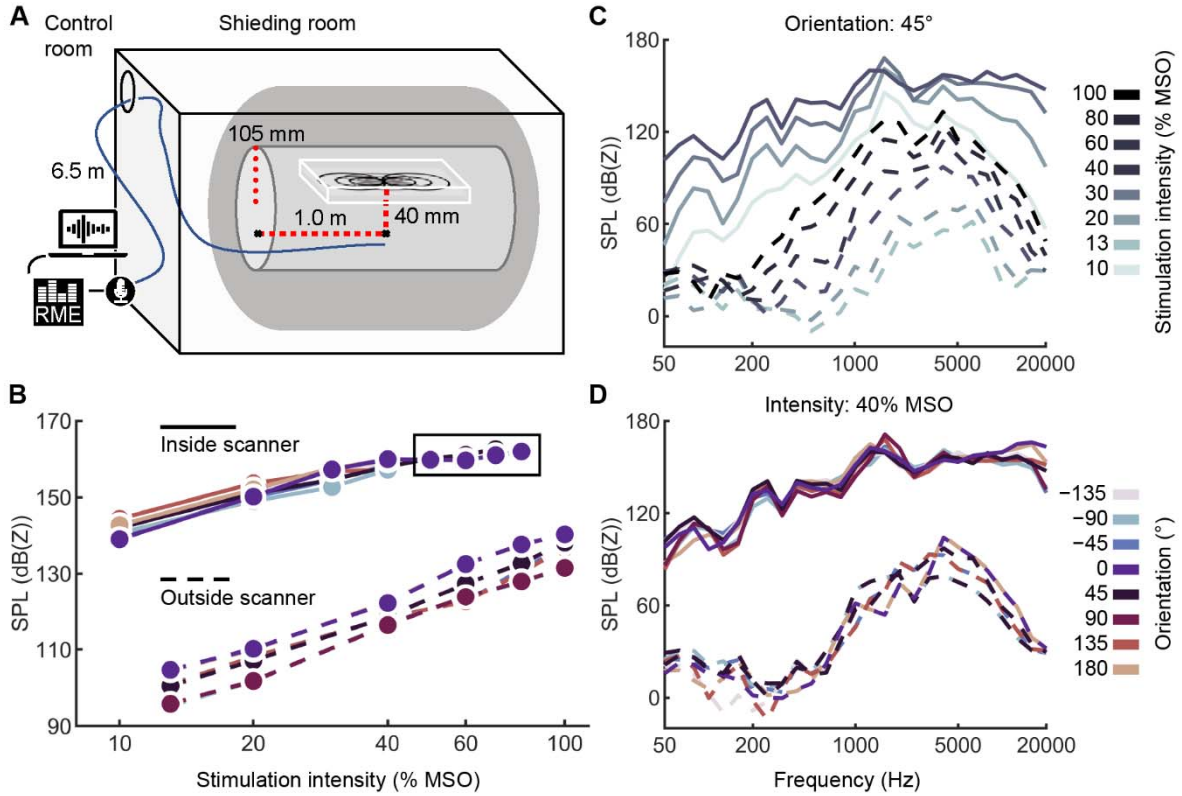

Fig. 6. Acoustic noise from the mTMS pulses. (**A**) The acoustic noise measurement setup inside the MRI bore with the open end of the measurement tube pointing towards the transducer and

placed inside the MRI bore in the two positions indicated by the black dots connected with red dashed lines for 1) near-field and 2) far-field measurements. The tube orientation and position in the image are for illustration purposes only. (**B**) Peak SPLs measured outside and inside the MRI scanner with the open end of the tube at 4 cm below the transducer with different stimulation intensities and orientations. The measurement points inside the square were performed using an earplug as a dampener at the open end of the tube. (**C**) 1/3 octave spectra of the acoustic noise from mTMS pulses at 45° orientation (bottom and top coils together) for different intensities. (**D**) 1/3 octave spectra for mTMS pulses at 40% MSO with varying stimulus orientations. Dashed and solid lines indicate measurements outside and inside the MRI scanner, respectively.

Effects of stimulus orientation on motor response

We observed that the MEP amplitude considerably depended on the stimulated brain hemisphere and the E-field orientation (Fig. 7A–B). On the right brain hemisphere, contralateral MEPs with the highest amplitudes were evoked at −90°, −45°, 90°, and 135°, while no MEPs were detected at the remaining orientations. In turn, the left hemisphere showed the highest contralateral MEP amplitudes for mTMS pulses at 45°, 90°, and −135°, with no MEPs at −90°, −45°, and 180° (Fig. 7D). We detected ipsi- and contralateral MEPs in both hemispheres with latencies of about 10 ms (Fig. 7E).

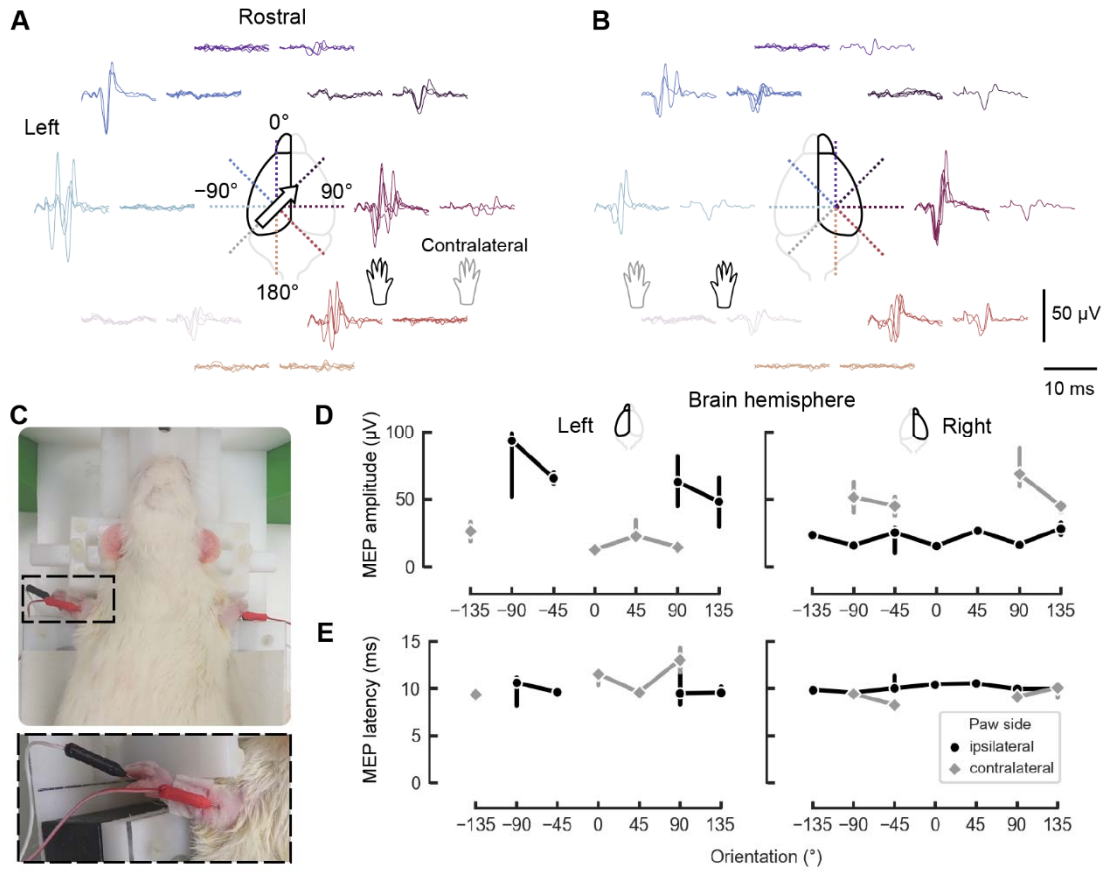

Fig. 7. Effect of mTMS pulse orientation on MEPs. MEPs recorded from the rat's left and right biceps brachii with mTMS pulses on the (**A**) left and (**B**) right rat brain hemispheres. (**C**) Photos depicting the rat placement on the holder and the needle electrode placement on the right and left front paws. The dashed square highlights the electrode placement. (**D**) MEP amplitude from ipsilateral (black circle) and contralateral (gray diamond) paws after stimulation of the rat's left and right brain hemispheres with stimulus orientations from −135° to 180°. Markers represent the medians across trials, and the error bars represent the 95% confidence interval. (**E**) Latency for the corresponding MEP amplitudes. Missing latency values result from MEPs with zero amplitude or trials rejected during signal preprocessing. The biggest contralateral MEPs were recorded with mTMS pulses on the right brain hemisphere (**B**) and with the E-field orientations 45°, 90°, 135°, and −90°.

Discussion

We introduce and demonstrate the first in-situ mTMS–MRI setup for concurrent stimulation and imaging of small animals in an ultra-high-field MRI scanner (9.4-T static field). The electronic control of TMS stimulus parameters with the transducer inside the MRI bore solves important limitations of concurrent TMS–MRI applications. For instance, with specialized multi-coil transducers [47], distinct cortical areas can be subsequently targeted within milliseconds with interleaved imaging sequences, allowing causal assessment of network brain functions [3]. With electronic targeting, we also minimize the need for physical repositioning of the stimulating coil. Such repositioning requires the operator to remove the experimental setup away from the bore, which is time-consuming and prone to errors.

The mTMS–MRI installation with the cabinet inside the shielded room and the control unit outside provides significant advantages compared to existing systems [43,44]. This installation minimizes the length of the transducer cabling, whereas commercial MRI-compatible TMS systems typically utilize extra-long coil cables and introduce the coil into the MRI room via a waveguide combined with a low-pass filter. This has been reported to result in a loss of up to 15% in stimulation strength [14]. The stimulation intensity is a critical limiting factor in TMS in preclinical applications due to the reduced electromagnetic coupling between the animal's brain and the stimulation coils. Thus, even minor improvements in stimulation intensity might enable a broader range of stimulation protocols. Another crucial improvement is that the computer used to control the mTMS device from the MRI control room allows flexible programming of mTMS pulse waveforms and sequence protocols. This feature eliminates the need for the operator to frequently enter and exit the shielded room during experimental sessions, reducing exposure to potential health risks, such as electric hazards and high acoustic noise levels (discussed below).

A unique characteristic of our system is the electronic control of the E-field orientation in the rat cortex enabled by the 2-coil mTMS transducer inside the MRI bore. We combined rigid polycarbonate plates with a layer of fluoroelastomer and potting with a special silicone for improved impact absorption. This layered design withstood stimulation intensities up to 80% of MSO in all orientations. This is a significant improvement compared to our first prototypes manufactured with only polyoxymethylene (POM) and potted with epoxy, which fractured at about 40% MSO. Further research is still required to achieve more durable, efficient, quiet, and, if desired, more focal stimulation coils. In applications not requiring high focality, it might be best to trade the focality fully for efficiency [52], as such coils can evoke reliable MEPs in rats with relaxed durability requirements [53]. Importantly, the multi-channel TMS system is flexible and can be utilized with multiple coil array combinations designed for specific purposes, such as precise electronic cortical mapping [47,54].

Our phantom measurements indicate that the MRI-compatible mTMS system is suitable for conventional preclinical MRI studies. With charged mTMS pulse capacitors, the stimulation coils inside the bore induced minimal changes in the FID signal, indicating that the coil cables did introduce high-frequency noise, and the potential small leakage current from the high-voltage capacitors had a minimal effect. We did not observe any significant image distortions, and there was only a small signal originating from the mTMS transducer in commonly used gradient and spin echo sequences. In addition, only a 6-ms delay was required after the mTMS pulse to have a negligible effect on the FID data. We should note that our mTMS–MRI delay measurements were conducted only up to 25% MSO. However, based on a logarithm extrapolation, the required delays are within 10–20 ms for higher voltages (e.g., 67% MSO). This delay range is suitable for interleaved mTMS–MRI recordings and lower than the minimum reported in previous studies, in

which 50–100 ms have been suggested to avoid TMS artifacts in echo planar images [43,44]. An evident limitation of our study is that no TMS-evoked functional MRI signals were measured from the rat's brain. Such measurement falls outside this study's scope and could potentially lead to unnecessary complexities in interpreting the neurophysiological effects of brain stimulation that would be better explored in a future study.

The SPL increased logarithmically with increased stimulation intensity, and there were small differences depending on the stimulation orientations. At a 1-m distance from the coil, the acoustic noise levels were about 20–23 dB lower than at a 4-cm distance, so proper safety measures must be in place to prevent accidental mTMS pulses when personnel are working close to the bore, for example, during the preparation of the animal for the experiment. The safety limit for the peak SPL for humans (140 dB(C), computed with C-weighting) was exceeded during stimulation both outside and inside the MRI bore. Still, it remained at safe levels in the operation room. In general, laboratory animals exposed to continuous sound suffer from the same reactions to noise ranging from auditory effects like temporary or permanent threshold shifts and tinnitus to non-auditory effects emerging from noise-induced stress, such as elevated heart rate and sleeping problems [55,56]. Experiments with mTMS in an ultra-high-field MRI should be performed with anesthetized animals, as in this study, carefully considering the animal safety regarding exposure to impulse sounds.

As a proof of concept of the electronic control of stimulus orientation, we demonstrated that the MEPs considerably depended on the E-field orientation. The corresponding MEP latencies (approximately 10 ms) are akin to those reported in previous studies [49,50,53]. Interestingly, only specific transducer locations and orientations generated MEPs despite the relatively broad induced E-fields (20–30 mm range), which, in principle, would stimulate large cortical areas.

This is further supported by the similarity of the MEPs across different orientations evoked by stimulation of both right and left hemispheres (see Fig. 7A–B), as it is likely that both transducer locations stimulated the same cortical region due to the widespread electric field patterns on the rat's cortical surface [57]. Such high TMS spatial and orientation specificity could be due to a localized motor cortical representation by neuronal ensembles aligned in laminar and columnar structures [58], as extensively studied in humans [39,59,60], and further supported by the stimulation of subcortical neuronal pathways with deep brain stimulation electrodes [61,62]. Future studies with more focal E-fields would better elucidate the underlying physiological and anatomical processes on the orientation sensitivity of the rat brain motor representations.

Conclusion

In conclusion, our system enables concurrent non-invasive neuroimaging and brain stimulation applications in a preclinical setting. This setup can be utilized to create and test a wide range of protocols to study the whole-brain network effects of neuromodulation [4,14,32,63] and treatments for neurological disorders [3,7,33].

Acknowledgments

This project has received funding from the Jane and Aatos Erkko Foundation, the Academy of Finland (decisions No. 294625 and 349985), and the European Research Council (ERC Synergy) under the European Union's Horizon 2020 research and innovation programme (ConnectToBrain; grant agreement No 810377). We acknowledge the computational resources provided by the Aalto Science-IT project.

Conflicts of interest

RJI is an advisor and a minority shareholder of Nexstim Plc. JON and RJI are inventors of patents on mTMS technology. All other authors declare they have no competing interests.

References

[1] Lynn CW, Bassett DS. The physics of brain network structure, function and control. Nature Reviews Physics 2019;1:318–32. https://doi.org/10.1038/s42254-019-0040-8.

[2] Betzel RF, Bassett DS. Multi-scale brain networks. Neuroimage 2017;160:73–83. https://doi.org/10.1016/j.neuroimage.2016.11.006.

[3] Siddiqi SH, Kording KP, Parvizi J, Fox MD. Causal mapping of human brain function. Nat Rev Neurosci 2022;23:361–75. https://doi.org/10.1038/s41583-022-00583-8.

[4] Yang Y, Qiao S, Sani OG, Sedillo JI, Ferrentino B, Pesaran B, et al. Modelling and prediction of the dynamic responses of large-scale brain networks during direct electrical stimulation. Nat Biomed Eng 2021;5:324–45. https://doi.org/10.1038/s41551-020-00666-w.

[5] Gordon EM, Chauvin RJ, Van AN, Rajesh A, Nielsen A, Newbold DJ, et al. A somato-cognitive action network alternates with effector regions in motor cortex. Nature 2023;617:351–9. https://doi.org/10.1038/s41586-023-05964-2.

[6] Tang W, Choi EY, Heilbronner SR, Haber SN. Nonhuman primate meso-circuitry data: a translational tool to understand brain networks across species. Brain Structure and Function 2020 226:1 2020;226:1–11. https://doi.org/10.1007/S00429-020-02133-3.

[7] Dawson TM, Golde TE, Lagier-Tourenne C. Animal models of neurodegenerative diseases. Nat Neurosci 2018;21:1370–9. https://doi.org/10.1038/s41593-018-0236-8.

[8] Tang A, Thickbroom G, Rodger J. Repetitive transcranial magnetic stimulation of the brain. The Neuroscientist 2017;23:82–94. https://doi.org/10.1177/1073858415618897.

[9] Surendrakumar S, Rabelo TK, Campos ACP, Mollica A, Abrahao A, Lipsman N, et al. Neuromodulation therapies in pre-clinical models of traumatic brain injury: Systematic review and translational applications. J Neurotrauma 2023;40:435–48. https://doi.org/10.1089/neu.2022.0286.

[10] Nestler EJ, Hyman SE. Animal models of neuropsychiatric disorders. Nat Neurosci 2010;13:1161–9. https://doi.org/10.1038/nn.2647.

[11] Allen EA, Pasley BN, Duong T, Freeman RD. Transcranial magnetic stimulation elicits coupled neural and hemodynamic consequences. Science (1979) 2007;317:1918–21. https://doi.org/10.1126/science.1146426.

[12] Ilmoniemi RJ, Virtanen J, Ruohonen J, Karhu J, Aronen HJ, Näätänen R, et al. Neuronal responses to magnetic stimulation reveal cortical reactivity and connectivity. Neuroreport 1997;8:3537–40. https://doi.org/10.1097/00001756-199711100-00024.

[13] Siebner HR, Bergmann TO, Bestmann S, Massimini M, Johansen-Berg H, Mochizuki H, et al. Consensus paper: Combining transcranial stimulation with neuroimaging. Brain Stimul 2009;2:58–80. https://doi.org/10.1016/j.brs.2008.11.002.

[14] Bergmann TO, Varatheeswaran R, Hanlon CA, Madsen KH, Thielscher A, Siebner HR. Concurrent TMS-fMRI for causal network perturbation and proof of target engagement. Neuroimage 2021;237:118093. https://doi.org/10.1016/j.neuroimage.2021.118093.

[15] Siddiqi SH, Schaper FLWVJ, Horn A, Hsu J, Padmanabhan JL, Brodtmann A, et al. Brain stimulation and brain lesions converge on common causal circuits in neuropsychiatric disease. Nat Hum Behav 2021;5:1707–16. https://doi.org/10.1038/s41562-021-01161-1.

[16] Sydnor VJ, Cieslak M, Duprat R, Deluisi J, Flounders MW, Long H, et al. Cortical-subcortical structural connections support transcranial magnetic stimulation engagement of the amygdala. Sci Adv 2022;8:5803. https://doi.org/10.1126/sciadv.abn5803.

[17] Cash RFH, Weigand A, Zalesky A, Siddiqi SH, Downar J, Fitzgerald PB, et al. Using brain imaging to improve spatial targeting of transcranial magnetic stimulation for depression. Biol Psychiatry 2021;90:689–700. https://doi.org/10.1016/J.BIOPSYCH.2020.05.033.

[18] Siddiqi SH, Taylor JJ, Horn A, Fox MD. Bringing Human Brain Connectomics to Clinical Practice in Psychiatry. Biol Psychiatry 2023;93:386–7. https://doi.org/10.1016/j.biopsych.2022.05.026.

[19] Lefaucheur J-P, André-Obadia N, Antal A, Ayache SS, Baeken C, Benninger DH, et al. Evidence-based guidelines on the therapeutic use of repetitive transcranial magnetic stimulation (rTMS). Clinical Neurophysiology 2014;125:1–57. https://doi.org/10.1016/j.clinph.2014.05.021.

[20] Funke K. Transcranial Magnetic Stimulation of Rodents. Handb Behav Neurosci, vol. 28, Elsevier; 2018, p. 365–87. https://doi.org/10.1016/B978-0-12-812028-6.00020-3.

[21] Krieg TD, Salinas FS, Narayana S, Fox PT, Mogul DJ. PET-based confirmation of orientation sensitivity of TMS-induced cortical activation in humans. Brain Stimul 2013;6:898–904. https://doi.org/10.1016/j.brs.2013.05.007.

[22] Tastevin M, Richieri R, Boyer L, Fond G, Lançon C, Guedj E. Brain PET metabolic substrate of TMS response in pharmaco-resistant depression. Brain Stimul 2020;13:683–5. https://doi.org/10.1016/j.brs.2020.02.014.

[23] Wyckhuys T, De Geeter N, Crevecoeur G, Stroobants S, Staelens S. Quantifying the effect of repetitive transcranial magnetic stimulation in the rat brain by μsPECT CBF scans. Brain Stimul 2013;6:554–62. https://doi.org/10.1016/J.BRS.2012.10.004.

[24] Parthoens J, Wyckhuys T, Crevecoeur G, Stroobants S, Staelens S. Fast screening of transcranial magnetic stimulation paradigms in the rat using microPET. Journal of Nuclear Medicine 2012;53.

[25] El Arfani A, Parthoens J, Demuyser T, Servaes S, De Coninck M, De Deyn PP, et al. Accelerated high-frequency repetitive transcranial magnetic stimulation enhances motor activity in rats. Neuroscience 2017;347:103–10. https://doi.org/10.1016/j.neuroscience.2017.01.045.

[26] Paus T, Jech R, Thompson CJ, Comeau R, Peters T, Evans AC. Transcranial magnetic stimulation during positron emission tomography: A new method for studying connectivity of the human cerebral cortex. The Journal of Neuroscience 1997;17:3178–84. https://doi.org/10.1523/JNEUROSCI.17-09-03178.1997.

[27] Massimini M, Ferrarelli F, Huber R, Esser SK, Singh H, Tononi G. Breakdown of cortical effective connectivity during sleep. Science (1979) 2005;309:2228–32. https://doi.org/10.1126/science.1117256.

[28] Rosanova M, Casali A, Bellina V, Resta F, Mariotti M, Massimini M. Natural frequencies of human corticothalamic circuits. Journal of Neuroscience 2009;29:7679–85. https://doi.org/10.1523/JNEUROSCI.0445-09.2009.

[29] Li L, Yin Z, Huo X. The influence of low-frequency rTMS on EEG of rats. Neurosci Lett 2007;412:143–7. https://doi.org/10.1016/j.neulet.2006.10.054.

[30] Rotenberg A, Muller P, Birnbaum D, Harrington M, Riviello JJ, Pascual-Leone A, et al. Seizure suppression by EEG-guided repetitive transcranial magnetic stimulation in the rat. Clinical Neurophysiology 2008;119:2697–702. https://doi.org/10.1016/j.clinph.2008.09.003.

[31] Bergmann TO, Karabanov A, Hartwigsen G, Thielscher A, Siebner HR. Combining non-invasive transcranial brain stimulation with neuroimaging and electrophysiology: Current approaches and future perspectives. Neuroimage 2016;140:4–19. https://doi.org/10.1016/j.neuroimage.2016.02.012.

[32] Tik M, Woletz M, Schuler A-L, Vasileiadi M, Cash RFH, Zalesky A, et al. Acute TMS/fMRI response explains offline TMS network effects – An interleaved TMS-fMRI study. Neuroimage 2023;267:119833. https://doi.org/10.1016/j.neuroimage.2022.119833.

[33] Seewoo BJ, Etherington SJ, Feindel KW, Rodger J. Combined rTMS/fMRI Studies: An Overlooked Resource in Animal Models. Front Neurosci 2018;12. https://doi.org/10.3389/fnins.2018.00180.

[34] Mizutani-Tiebel Y, Tik M, Chang K-Y, Padberg F, Soldini A, Wilkinson Z, et al. Concurrent TMS-fMRI: Technical challenges, developments, and overview of previous studies. Front Psychiatry 2022;13:581. https://doi.org/10.3389/fpsyt.2022.825205.

[35] Lee H-J, Woudsma KJ, Ishraq MF, Lin F-H. Design of coil holder for the improved maneuvering in concurrent TMS-MRI. Brain Stimul 2023;16:966–8. https://doi.org/10.1016/j.brs.2023.06.001.

[36] Nieminen JO, Koponen LM, Mäkelä N, Souza VH, Stenroos M, Ilmoniemi RJ. Short-interval intracortical inhibition in human primary motor cortex: A multi-locus transcranial magnetic stimulation study. Neuroimage 2019;203:116194. https://doi.org/10.1016/j.neuroimage.2019.116194.

[37] Tugin S, Souza VH, Nazarova MA, Novikov PA, Tervo AE, Nieminen JO, et al. Effect of stimulus orientation and intensity on short-interval intracortical inhibition (SICI) and facilitation (SICF): A multi-channel transcranial magnetic stimulation study. PLoS One 2021;16:e0257554. https://doi.org/10.1371/journal.pone.0257554.

[38] Crowther LJ, Porzig K, Hadimani RL, Brauer H, Jiles DC. Realistically modeled transcranial magnetic stimulation coils for lorentz force and stress calculations during MRI. IEEE Trans Magn 2013;49:3426–9. https://doi.org/10.1109/TMAG.2013.2247578.

[39] Souza VH, Nieminen JO, Tugin S, Koponen LM, Baffa O, Ilmoniemi RJ. TMS with fast and accurate electronic control: Measuring the orientation sensitivity of corticomotor pathways. Brain Stimul 2022;15:306–15. https://doi.org/10.1016/J.BRS.2022.01.009.

[40] Nieminen JO, Sinisalo H, Souza VH, Malmi M, Yuryev M, Tervo AE, et al. Multi-locus transcranial magnetic stimulation system for electronically targeted brain stimulation. Brain Stimul 2022;15:116–24. https://doi.org/10.1016/j.brs.2021.11.014.

[41] Navarro de Lara LI, Daneshzand M, Mascarenas A, Paulson D, Pratt K, Okada Y, et al. A 3-axis coil design for multichannel TMS arrays. Neuroimage 2021;224:117355. https://doi.org/10.1016/j.neuroimage.2020.117355.

[42] Navarro de Lara LI, Stockmann JP, Meng Q, Keil B, Mareyam A, Uluç I, et al. A novel whole-head RF coil design tailored for concurrent multichannel brain stimulation and imaging at 3T. Brain Stimul 2023;16:1021–31. https://doi.org/10.1016/j.brs.2023.05.025.

[43] Navarro de Lara LI, Tik M, Woletz M, Frass-Kriegl R, Moser E, Laistler E, et al. High-sensitivity TMS/fMRI of the human motor cortex using a dedicated multichannel MR coil. Neuroimage 2017;150:262–9. https://doi.org/10.1016/j.neuroimage.2017.02.062.

[44] Bestmann S, Baudewig J, Frahm J. On the synchronization of transcranial magnetic stimulation and functional echo-planar imaging. Journal of Magnetic Resonance Imaging 2003;17:309–16. https://doi.org/10.1002/jmri.10260.

[45] Koponen LM, Nieminen JO, Mutanen TP, Stenroos M, Ilmoniemi RJ. Coil optimisation for transcranial magnetic stimulation in realistic head geometry. Brain Stimul 2017;10:795–805. https://doi.org/10.1016/j.brs.2017.04.001.

[46] Koponen LM, Nieminen JO, Ilmoniemi RJ. Multi-locus transcranial magnetic stimulation—theory and implementation. Brain Stimul 2018;11:849–55. https://doi.org/10.1016/j.brs.2018.03.014.

[47] Rissanen IJ, Souza VH, Nieminen JO, Koponen LM, Ilmoniemi RJ. Advanced pipeline for designing multi-locus TMS coils with current density constraints. IEEE Trans Biomed Eng 2023;70:2025–34. https://doi.org/10.1109/TBME.2023.3234119.

[48] Nieminen JO, Koponen LM, Ilmoniemi RJ. Experimental characterization of the electric field distribution induced by TMS devices. Brain Stimul 2015;8:582–9. https://doi.org/10.1016/j.brs.2015.01.004.

[49] Rotenberg A, Muller PA, Vahabzadeh-Hagh AM, Navarro X, López-Vales R, Pascual-Leone A, et al. Lateralization of forelimb motor evoked potentials by transcranial magnetic stimulation in rats. Clinical Neurophysiology 2010;121:104–8. https://doi.org/10.1016/j.clinph.2009.09.008.

[50] Boonzaier J, Petrov PI, Otte WM, Smirnov N, Neggers SFW, Dijkhuizen RM. Design and evaluation of a rodent-specific transcranial magnetic stimulation coil: An in silico and in vivo validation study. Neuromodulation: Technology at the Neural Interface 2020;23:324–34. https://doi.org/10.1111/ner.13025.

[51] Acoustical Society of America. American National Standard Electroacoustics - Sound level meters - Part 1: Specifications (a nationally adopted international standard) - ANSI/ASA S1.4-2014/Part 1. IEC 61672-1:2013. Melville, NY: Acoustical Society of America; 2014.

[52] Nurmi S, Karttunen J, Souza VH, Ilmoniemi RJ, Nieminen JO. Trade-off between stimulation focality and the number of coils in multi-locus transcranial magnetic stimulation. J Neural Eng 2021;18:066003. https://doi.org/10.1088/1741-2552/ac3207.

[53] Nieminen JO, Pospelov AS, Koponen LM, Yrjölä P, Shulga A, Khirug S, et al. Transcranial magnetic stimulation set-up for small animals. Front Neurosci 2022;16. https://doi.org/10.3389/fnins.2022.935268.

[54] Nieminen JO, Sinisalo H, Souza VH, Malmi M, Yuryev M, Tervo AE, et al. Multi-locus transcranial magnetic stimulation system for electronically targeted brain stimulation. Brain Stimul 2022;15:116–24. https://doi.org/10.1016/j.brs.2021.11.014.

[55] Lauer AM, El-Sharkawy A-MM, Kraitchman DL, Edelstein WA. MRI acoustic noise can harm experimental and companion animals. Journal of Magnetic Resonance Imaging 2012;36:743–7. https://doi.org/10.1002/jmri.23653.

[56] Turner JG, Bauer CA, Rybak LP. Noise in animal facilities: why it matters. J Am Assoc Lab Anim Sci 2007;46:10–3.

[57] Koponen LM, Stenroos M, Nieminen JO, Jokivarsi K, Gröhn O, Ilmoniemi RJ. Individual head models for estimating the TMS-induced electric field in rat brain. Sci Rep 2020;10:17397. https://doi.org/10.1038/s41598-020-74431-z.

[58] Kätzel D, Zemelman B V, Buetfering C, Wölfel M, Miesenböck G. The columnar and laminar organization of inhibitory connections to neocortical excitatory cells. Nat Neurosci 2011;14:100–7. https://doi.org/10.1038/nn.2687.

[59] Fox PT, Narayana S, Tandon N, Sandoval H, Fox SP, Kochunov P, et al. Column-based model of electric field excitation of cerebral cortex. Hum Brain Mapp 2004;22:1–14. https://doi.org/10.1002/hbm.20006.

[60] Weise K, Numssen O, Kalloch B, Zier AL, Thielscher A, Haueisen J, et al. Precise motor mapping with transcranial magnetic stimulation. Nat Protoc 2023;18:293–318. https://doi.org/10.1038/s41596-022-00776-6.

[61] Lehto LJ, Canna A, Wu L, Sierra A, Zhurakovskaya E, Ma J, et al. Orientation selective deep brain stimulation of the subthalamic nucleus in rats. Neuroimage 2020;213:116750. https://doi.org/10.1016/j.neuroimage.2020.116750.

[62] Slopsema JP, Peña E, Patriat R, Lehto LJ, Gröhn O, Mangia S, et al. Clinical deep brain stimulation strategies for orientation-selective pathway activation. J Neural Eng 2018;15:056029. https://doi.org/10.1088/1741-2552/aad978.

[63] Mengotti P, Käsbauer A-S, Fink GR, Vossel S. Combined TMS-fMRI reveals behavior-dependent network effects of right temporoparietal junction neurostimulation in an attentional belief updating task. Cerebral Cortex 2022;32:4698–714. https://doi.org/10.1093/cercor/bhab511.